SINTEF
PROCEEDINGS
2

Proceedings of the 12th International Conference on Computational Fluid Dynamics in the Oil & Gas, Metallurgical and Process Industries

Progress in Applied CFD – CFD2017

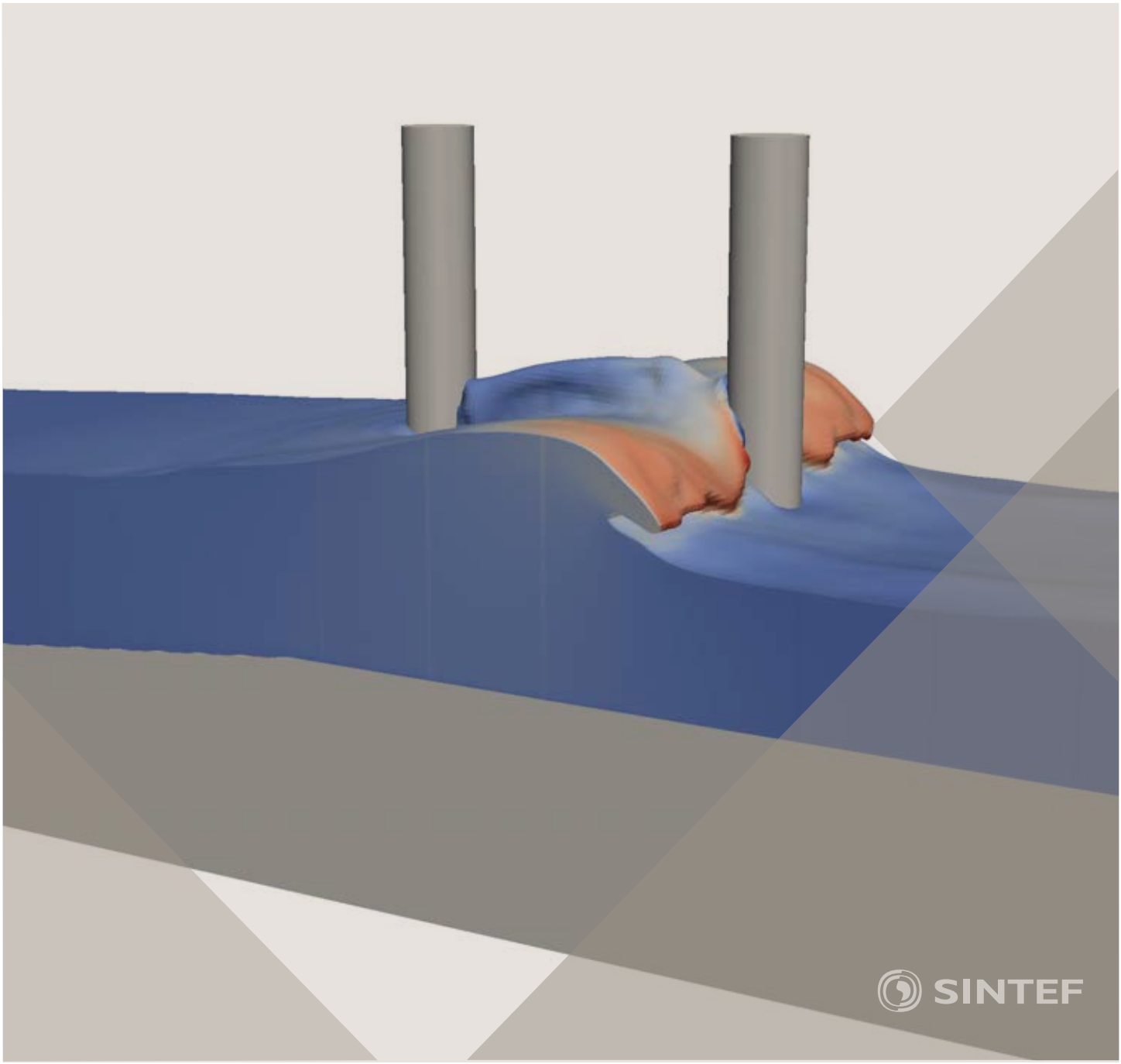

SINTEF Proceedings

Editors:
Jan Erik Olsen and Stein Tore Johansen

Progress in Applied CFD – CFD2017

Proceedings of the 12th International Conference on Computational Fluid Dynamics in the Oil & Gas, Metallurgical and Process Industries

SINTEF Academic Press

SINTEF Proceedings no 2
Editors: Jan Erik Olsen and Stein Tore Johansen
Progress in Applied CFD – CFD2017
Selected papers from 10th International Conference on Computational Fluid Dynamics in the Oil & Gas, Metallurgical and Process Industries

Key words:
CFD, Flow, Modelling

Cover, illustration: Arun Kamath

ISSN 2387-4295 (online)
ISBN 978-82-536-1544-8 (pdf)

SINTEF Academic Press
Address: Forskningsveien 3 B
PO Box 124 Blindern
N-0314 OSLO
Tel: +47 73 59 30 00
Fax: +47 22 96 55 08

www.sintef.no/byggforsk
www.sintefbok.no

SINTEF Proceedings
SINTEF Proceedings is a serial publication for peer-reviewed conference proceedings on a variety of scientific topics.
The processes of peer-reviewing of papers published in SINTEF Proceedings are administered by the conference organizers and proceedings editors. Detailed procedures will vary according to custom and practice in each scientific community.

PREFACE

This book contains all manuscripts approved by the reviewers and the organizing committee of the 12th International Conference on Computational Fluid Dynamics in the Oil & Gas, Metallurgical and Process Industries. The conference was hosted by SINTEF in Trondheim in May/June 2017 and is also known as CFD2017 for short. The conference series was initiated by CSIRO and Phil Schwarz in 1997. So far the conference has been alternating between CSIRO in Melbourne and SINTEF in Trondheim. The conferences focuses on the application of CFD in the oil and gas industries, metal production, mineral processing, power generation, chemicals and other process industries. In addition pragmatic modelling concepts and bio-mechanical applications have become an important part of the conference. The papers in this book demonstrate the current progress in applied CFD.

The conference papers undergo a review process involving two experts. Only papers accepted by the reviewers are included in the proceedings. 108 contributions were presented at the conference together with six keynote presentations. A majority of these contributions are presented by their manuscript in this collection (a few were granted to present without an accompanying manuscript).

The organizing committee would like to thank everyone who has helped with review of manuscripts, all those who helped to promote the conference and all authors who have submitted scientific contributions. We are also grateful for the support from the conference sponsors: ANSYS, SFI Metal Production and NanoSim.

Stein Tore Johansen & Jan Erik Olsen

Organizing committee:

Conference chairman: Prof. Stein Tore Johansen
Conference coordinator: Dr. Jan Erik Olsen
Dr. Bernhard Müller
Dr.Sigrid Karstad Dahl
Dr.Shahriar Amini
Dr.Ernst Meese
Dr.Josip Zoric
Dr.Jannike Solsvik
Dr.Peter Witt

Scientific committee:

Stein Tore Johansen, SINTEF/NTNU
Bernhard Müller, NTNU
Phil Schwarz, CSIRO
Akio Tomiyama, Kobe University
Hans Kuipers, Eindhoven University of Technology
Jinghai Li, Chinese Academy of Science
Markus Braun, Ansys
Simon Lo, CD-adapco
Patrick Segers, Universiteit Gent
Jiyuan Tu, RMIT
Jos Derksen, University of Aberdeen
Dmitry Eskin, Schlumberger-Doll Research
Pär Jönsson, KTH
Stefan Pirker, Johannes Kepler University
Josip Zoric, SINTEF

CONTENTS

DIRECT NUMERICAL SIMULATION OF COUPLED HEAT AND MASS TRANSFER IN FLUID-SOLID SYSTEMS

Jiangtao Lu* , E.A.J.F. Peters, J.A.M. Kuipers

Multiphase Reactors Group, Department of Chemical Engineering and Chemistry, Eindhoven University of Technology, P.O. Box 513, 5600 MB Eindhoven, The Netherlands

* E-mail: J.Lu1@tue.nl

ABSTRACT

In this paper, an efficient ghost-cell based immersed boundary method is introduced to perform direct numerical simulation (DNS) of particulate flows. The fluid-solid coupling is achieved by implicit incorporation of the boundary conditions into the discretized momentum, thermal and species conservation equations of the fluid phase. Taking the advantage of a second order quadratic interpolation scheme, different boundary conditions could be realized consistently in our ghost-cell based immersed boundary method. The heat and mass transport in a fluid-particle system is coupled through the solid temperature, which offers a dynamic boundary condition for the fluid thermal equation.

The present simulations are performed for three different fluid-solid systems. The first one is the unsteady mass and heat diffusion in a large pool of quiescent fluid. The solution of the solid temperature development obtained from DNS is compared with the "exact" solution obtained from a standard second-order finite difference technique. Following that, we consider a stationary sphere under forced convection. The steady state temperature of the particle can be calculated from the fluid-solid mass and heat transfer rates, which are obtained from the well-known empirical Ranz-Marshall and Frössling correlations. The last simulation case is an in-line array of three spheres, the so-called three-bead reactor. The computed adiabatic temperature rise obtained from DNS shows good agreement with the value calculated from the overall species conversion ratio of the reactor.

Keywords: Direct numerical simulation, ghost-cell based immersed boundary method, particulate flows, multiphase heat and mass transfer.

NOMENCLATURE

Greek Symbols

α, β	Coefficients of Robin boundary condition.
α_h	Heat transfer coefficient, [W/m^2/K].
λ_f	Fluid thermal conductivity, [W/m/K].
μ_f	Fluid dynamic viscosity, [kg/m/s].
ξ_f	Species conversion ratio, [1].
ρ_f	Fluid density, [kg/m^3].
ϕ	General fluid variable.
ΔH_r	Reaction enthalpy, [J/mol].
Δt	Time step, [s].
ΔT_a	Adiabatic temperature rise, [K].
$\Phi_{h,f\to s}$	Heat transfer rate from fluid to solid, [J/s].
$\Phi_{m,f\to s}$	Molar transfer rate from fluid to solid, [mol/s].

Latin Symbols

a, b	Coefficients in generic discretised equations.
c_f	Molar concentration, [mol/m^3].
$c_{f,0}$	Initial molar concentration, [mol/m^3].
$c_{f,in}$	Inlet molar concentration, [mol/m^3].
c_{ijk}	Coefficients in second-order polynomial.
$C_{p,f}$	Fluid heat capacity, [J/kg/K].
$C_{p,s}$	Solid volumetric heat capacity, [J/m^3/K].
C_h	Convective heat transport per unit of volume, [W/m^3].
C_m	Convective species transport per unit of volume, [mol/m^3/s].
$\boldsymbol{C}_m$	Convective momentum flux, [N/m^3].
d_s	Sphere diameter, [m].
D_f	Mass diffusivity, [m^2/s].
D_h	Diffusive heat transport per unit of volume, [W/m^3].
D_m	Diffusive species transport per unit of volume, [mol/m^3/s].
$\boldsymbol{D}_m$	Diffusive momentum flux, [N/m^3].
f	Coefficient of Robin boundary condition.
$\boldsymbol{g}$	Gravitational acceleration, [m/s^2].
k_m	Mass transfer coefficient, [m/s].
$\boldsymbol{n}$	Unit normal vector, [1].
p	Pressure, [Pa].
r	Spherical coordinate, [m].
R_s	Sphere radius, [m].
S	Area, [m^2].
S_S	Particle surface area, [m^2].
t	Time, [s].
T_f	Fluid temperature, [K].
$T_{f,0}$	Initial fluid temperature, [K].
$T_{f,in}$	Inlet fluid temperature, [K].
$T_{f,out}$	Outlet fluid temperature, [K].
T_s	Solid temperature, [K].
$\boldsymbol{u}$	Velocity, [m/s].
V_s	Particle volume, [m^3].
x, y, z	Relative Cartesian coordinate, [m].

X, Y, Z Cartesian coordinate, [m].

Sub/superscripts
f Fluid phase.
s Solid phase.

INTRODUCTION

Fluid-particle flows are frequently encountered in a wide range of industrial processes, such as chemical, petrochemical and energy industries. Often these processes are accompanied with significant heat effects. Understanding the mass and heat transport processes in such complex heterogeneous systems is of great importance to improve performance and facilitate optimal design of process equipment.

For prediction of particulate flows in engineering scale equipment, accurate closures for fluid-solid interaction are of utmost importance. This requirement has led to the adoption of a multiscale modelling approach (van der Hoef *et al.* , 2008), which offers the possibility to compute and parameterize closures for application in more coarse-grained models. With the development of computational technology, DNS has become a powerful tool to resolve all the details at the smallest relevant length scales and quantitatively derive microscale transport coefficients to gain fundamental insight in fluid-solid interactions. In recent years the immersed boundary method (IBM), as a branch of DNS, has received a lot of attention. Taking the advantages of efficient CPU/memory utilization and easy grid generation, IBM is applied in various studies including complex situations of moving particles, complex geometries and deformable immersed objects (Fadlun *et al.* , 2000; Udaykumar *et al.* , 2001; Tseng and Ferziger, 2003). Following the fluid flow equations, additional equations for species and thermal energy transport can be added using the same methodology.

The IBM was first introduced by Peskin for simulation of blood around the flexible leaflet of a human heart (Peskin, 1977). The main idea of this method is to use a Cartesian grid for fluid flow simulation whereas the immersed boundary is represented by Lagrangian marker points. A forcing term is introduced to represent the interaction between the immersed boundary and the fluid, whose magnitude is taken such that the boundary conditions are fulfilled in an interpolated manner. A regularized Dirac delta function is used to distribute this singular force over a belt of cells surrounding each Lagrangian point. This method is categorized as continuous forcing method (CFM), and many researchers have contributed to the further development of this method (Goldstein *et al.* , 1993; Saiki and Biringen, 1996; Uhlmann, 2005). The second category of IBM is referred to as discrete forcing method (DFM), which was first proposed by Mohd-Yusof (1997), and later extended by Fadlun *et al.* (2000), Tseng and Ferziger (2003), Marella *et al.* (2005), Ghias *et al.* (2007), Haugen and Kragset (2010), Seo and Mittal (2011) and Lee and You (2013). In this method the ghost point approach is applied, where the virtual (i.e. inside the immersed body) variable value is calculated through the boundary condition and the fluid variables near the boundary. DFM treats the immersed boundary as a sharp interface, and does not require the explicit addition of a force in the governing equations, thus the stability limit is the same as that without the immersed boundaries.

Although IBM has been widely used for studies of momentum transfer in fluid-solid system, very few computational results are available in the field of mass and heat transfer (Bagchi *et al.* , 2000; Zhang *et al.* , 2008; Wang *et al.* , 2009; Shu *et al.* , 2013; Tavassoli *et al.* , 2013; Tenneti *et al.* , 2013; Xia *et al.* , 2014). Coupled mass and heat transfer has been reported by Dierich *et al.* (2011) using 2D DNS, Li *et al.* (2013) using Lattice Boltzmann method and Deen and Kuipers (2014) using 3D DNS with directional quadratic interpolation scheme.

In this paper, an efficient ghost-cell based immersed boundary method is proposed for the simulation of coupled heat and mass transfer problems in fluid-solid system. The reconstruction procedures involve a second order quadratic interpolation scheme. As the unique feature, different boundary conditions are realized consistently and enforced exactly at the particle surface. The organisation of this paper is as follows. First, the description of the model is given. Subsequently, the results are presented, through which the strength of our DNS model is demonstrated. Single sphere unsteady diffusion, forced convection to a single stationary sphere and a three-bead reactor are considered and analysed. Finally, the conclusions are presented.

MODEL DESCRIPTION

In this part, we describe the governing equations that need to be solved in DNS, the numerical details involved in the finite difference scheme, as well as the fluid-solid coupling. For the model presented in this paper, the following main assumptions are applied:

- The fluid phase is incompressible and Newtonian.
- The solid phase consists of spherical particles, and intra-particle temperature gradients are negligible.
- Both fluid and solid phase have constant physical properties.

Governing equations of fluid phase

The transport phenomena in the fluid phase are governed by the conservation equations for mass, momentum, species and thermal energy, respectively defined as:

$$\nabla \cdot \boldsymbol{u} = 0 \tag{1}$$

$$\frac{\partial \rho_f \boldsymbol{u}}{\partial t} + \nabla \cdot \left(\rho_f \boldsymbol{u}\boldsymbol{u} \right) = -\nabla p + \mu_f \nabla^2 \boldsymbol{u} + \rho_f \boldsymbol{g} \tag{2}$$

$$\frac{\partial c_f}{\partial t} + \nabla \cdot \left(c_f \boldsymbol{u} \right) = D_f \nabla^2 c_f \tag{3}$$

$$\rho_f C_{p,f} \left[\frac{\partial T_f}{\partial t} + \nabla \cdot \left(T_f \boldsymbol{u} \right) \right] = \lambda_f \nabla^2 T_f \tag{4}$$

In above equations, ρ_f is the fluid density, μ_f is the fluid viscosity, D_f is the species mass diffusivity in the fluid

whereas $C_{p,f}$ and λ_f are the heat capacity and thermal conductivity of the fluid phase respectively.

Governing equation of solid phase

The particle temperature is governed by the following equation with the assumption of a uniform particle temperature:

$$V_s C_{p,s} \frac{dT_s}{dt} = \Phi_{h,f\to s} + \Phi_{m,f\to s}\left(-\Delta H_r\right) \tag{5}$$

In this equation, the first term on the right hand side is the fluid-solid heat transfer rate while the second term represents the rate of reaction heat liberated from a chemical reaction. The heat transfer rate and mass transfer rate, with the normal pointing outward of the solid, are calculated by the following two equations respectively:

$$\Phi_{h,f\to s} = -\iint_{S_s}\left(-\lambda_f \nabla T_f \cdot \boldsymbol{n}\right) dS \tag{6}$$

$$\Phi_{m,f\to s} = -\iint_{S_s}\left(-D_f \nabla c_f \cdot \boldsymbol{n}\right) dS \tag{7}$$

Considering an exothermal chemical reaction proceeding at the exterior surface of the particles, the heat liberation is assumed to be rapidly transported to the interior of the particle with a negligible intra-particle temperature gradient. The coupling between the fluid thermal energy equation and the fluid species conservation equation is fulfilled through the particle thermal energy equation. In other words, the particle temperature of individual particle offers a dynamic boundary condition for the thermal energy equation of the fluid phase.

For longer times, the particle temperature will become constant, which implies the liberated reaction heat is fully carried away by the fluid. In this case, Equation (5) reduces to the following one which is often encountered in descriptions of coupled heat and mass transport phenomena.

$$\Phi_{m,f\to s}\left(-\Delta H_r\right) = -\Phi_{h,f\to s} \tag{8}$$

Numerical solution method

The governing equations are solved by a finite difference scheme implemented for a staggered Cartesian grid. The grid is defined in three dimensions (3D) with a uniform grid spacing in all three directions. Building on the work of Deen *et al.* (2012), the numerical solution of the equations described in previous section is acquired by using both high order discretization schemes and small computational stencils. The momentum equation is discretised in time by a first order Euler scheme:

$$\rho_f \boldsymbol{u}^{n+1} = \rho_f \boldsymbol{u}^n + \Delta t\left[-\nabla p^{n+1} - \left(\frac{3}{2}\boldsymbol{C}_m^n - \frac{1}{2}\boldsymbol{C}_m^{n-1}\right) + \boldsymbol{D}_m^{n+1} + \rho_f \boldsymbol{g}\right] \tag{9}$$

In this equation, n is the time step index. The convective and diffusive momentum fluxes $\boldsymbol{C}_m$ and $\boldsymbol{D}_m$ are calculated by the spatial discretization of:

$$\boldsymbol{C}_m = \rho_f\left(\nabla \cdot \boldsymbol{u}\boldsymbol{u}\right) \tag{10}$$

$$\boldsymbol{D}_m = \mu_f \nabla^2 \boldsymbol{u} \tag{11}$$

The solution of Equation (9) is achieved by using a two-step projection method where a tentative velocity field $\vec{u}^{**}$ is first computed by neglecting the pressure gradient contribution. As the second step, the velocity field at the new time step $n+1$ is obtained based on the new pressure gradient calculated from Poisson equation at time step $n+1$. For the interested reader, we refer for a more detailed description of this method to the work of Deen and Kuipers (2013).

The species and thermal energy convection-diffusion equations are temporally discretised in the same way as for the momentum equation, namely the Adams-Bashforth scheme is applied for the convective transport while the fully implicit Euler backward scheme is used for the diffusion term.

$$c_f^{n+1} = c_f^n + \Delta t\left[-\left(\frac{3}{2}C_m^n - \frac{1}{2}C_m^{n-1}\right) + D_m^{n+1}\right] \tag{12}$$

$$T_f^{n+1} = T_f^n + \frac{\Delta t}{\rho_f C_{p,f}}\left[-\left(\frac{3}{2}C_h^n - \frac{1}{2}C_h^{n-1}\right) + D_h^{n+1}\right] \tag{13}$$

with the convective species molar flux C_m and convective heat flux C_h given by:

$$C_m = \nabla\cdot\left(c_f \boldsymbol{u}\right) \tag{14}$$

$$C_h = \rho_f C_{p,f} \nabla\cdot\left(T_f \boldsymbol{u}\right) \tag{15}$$

and the diffusive molar flux D_m and diffusive heat flux D_h computed as:

$$D_m = D_f \nabla^2 c_f \tag{16}$$

$$D_h = \lambda_f \nabla^2 T_f \tag{17}$$

For momentum, species and thermal energy equations, the convection term is spatially discretized by a second-order total variation diminishing scheme, whereas the diffusion term is computed with a standard second-order central differencing scheme. The boundary condition is enforced at exactly the immersed boundary surface, which is handled at the level of the discretized equations and will be introduced in detail in next section.

The solid phase equation is solved after the fluid phase equations. The trapezoidal rule is used for the time integration, which maintains second order accuracy.

$$T_s^{n+1} = T_s^n + \frac{\Delta t}{V_s C_{p,s}}\left[\Phi_{h,f\to s}^{n+\frac{1}{2}} + \left(-\Delta H_r\right)\Phi_{m,f\to s}^{n+\frac{1}{2}}\right] \tag{18}$$

Fluid-solid coupling

The fluid-solid coupling constitutes the key element of our model. In order to impose variable boundary conditions in a sharp interface way, a ghost-cell based immersed boundary method is developed. The discretization of momentum, species and thermal energy equation leads to algebraic equations of the following generic form:

$$a_c \phi_c + \sum_1^6 a_{nb}\phi_{nb} = b_c \tag{19}$$

where ϕ is the fluid variable for which we want to find a solution, namely velocity, concentration and temperature

fields for momentum, species and thermal energy equation, respectively. This equation provides the relationship between any fluid quantity ϕ_c and its six neighbouring points indicated as ϕ_{nb}.

Since the surfaces of the immersed objects do not coincide with the mesh boundaries, we need a special treatment for the nodes near the fluid-solid interface. In our method, the first step is to identify all ghost points, which are defined as points inside the solid phase but having at least one neighbour in fluid phase. These points are used to obtain a solution of the governing equations for the exterior of the solid phase. The second step is to check every fluid node whether any of its six surrounding neighbours represents a ghost point. If this is the case, a boundary condition has to be applied.

Figure 1 demonstrates the quadratic interpolation scheme used in our model. It is given in a 2D domain for illustration purpose, in which the shadow in cross shape represents the initial computational stencil containing four neighbours. In the end, i.e. after imposing the boundary condition, G is removed from the stencil, while F_1 and F_2 are added to it. It should be noted that this reconstruction procedure is of best suitability in case the description of the gradient in the normal direction is required, specifically the non-homogeneous Neumann boundary condition encountered in species transport calculation.

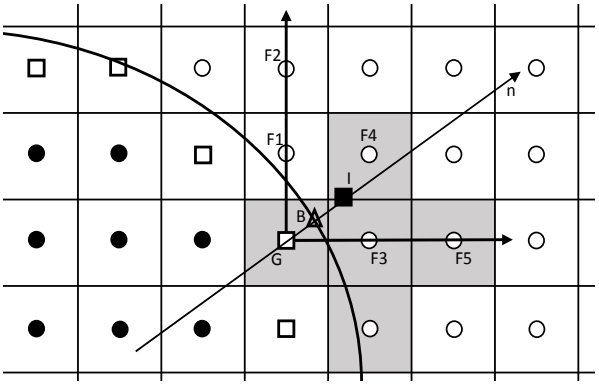

Figure 1: Schematic representation of the interpolation procedures for quadratic interpolation. Filled circles indicate the solid phase points, while open circles indicate the fluid phase points and open squares indicate the ghost points. The triangle and solid square are the boundary point and image point, respectively.

A generic variable ϕ in the vicinity of the immersed object surface could be approximated in terms of a second-order polynomial as follows:

$$\phi = \sum_{i=0}^{2}\sum_{j=0}^{2}\sum_{k=0}^{2} c_{ijk} x^i y^j z^k, i+j+k \le 2 \tag{20}$$

where relative coordinates are applied based on the location of boundary point (X_B, Y_B, Z_B), which is the interception of normal direction and immersed boundary surface.

$$x = X - X_B \tag{21}$$

$$y = Y - Y_B \tag{22}$$

$$z = Z - Z_B \tag{23}$$

Equation (20) is in fact the approximation of ϕ using the Taylor expansion near the boundary point:

$$\begin{aligned}\phi(x,y,z) &= \phi_B + \frac{\partial \phi_B}{\partial x}x + \frac{\partial \phi_B}{\partial y}y + \frac{\partial \phi_B}{\partial z}z \\ &+ \frac{1}{2}\frac{\partial^2 \phi_B}{\partial x^2}x^2 + \frac{1}{2}\frac{\partial^2 \phi_B}{\partial y^2}y^2 + \frac{1}{2}\frac{\partial^2 \phi_B}{\partial z^2}z^2 + \cdots\end{aligned} \tag{24}$$

In the 3D case, the number of coefficients for a second-order polynomial is ten. In order to determine these coefficients c_{ijk}, we need ϕ values from nine neighbouring fluid points and one image point. The image point is defined as the mirror point of the ghost point through the boundary in normal direction, which has the same distance to the boundary point as the ghost point. For the 2D case, only five fluid points plus one image point are required for computation of c_{ij} coefficients, as indicated in Figure 1.

With adequate data points (ten values at fluid/image point for ten coefficients in a second-order polynomial), the resulting equation for solving coefficients c_{ijk} can be written as a matrix vector multiplication:

$$\boldsymbol{\phi} = \boldsymbol{X}\boldsymbol{c} \tag{25}$$

where $\boldsymbol{\phi}$ and $\boldsymbol{c}$ are the vectors for species concentrations and coefficients respectively, and $\boldsymbol{X}$ is the Vandermonde matrix given by:

$$\boldsymbol{X} = \begin{bmatrix} 1 & x_1 & y_1 & z_1 & x_1^2 & y_1^2 & z_1^2 & x_1y_1 & x_1z_1 & y_1z_1 \\ 1 & x_2 & y_2 & z_2 & x_2^2 & y_2^2 & z_2^2 & x_2y_2 & x_2z_2 & y_2z_2 \\ & & & & & \vdots & & & & \\ 1 & x_{10} & y_{10} & z_{10} & x_{10}^2 & y_{10}^2 & z_{10}^2 & x_{10}y_{10} & x_{10}z_{10} & y_{10}z_{10} \end{bmatrix} \tag{26}$$

To solve Equation (25), the Vandermonde matrix is inversed by applying LU decomposition with Crout algorithm. The coefficients c_{ijk} are obtained by multiplication of the inversed matrix $\boldsymbol{X}^{-1}$ and the concentration vector $\boldsymbol{\phi}$, which can be written as a linear combination of ϕ values.

$$c_{000} = \phi_B = \sum_{m=1}^{10} \boldsymbol{X}_{1m}^{-1}\phi_m \tag{27}$$

$$c_{100} = \frac{\partial \phi_B}{\partial x} = \sum_{m=1}^{10} \boldsymbol{X}_{2m}^{-1}\phi_m \tag{28}$$

$$c_{010} = \frac{\partial \phi_B}{\partial y} = \sum_{m=1}^{10} \boldsymbol{X}_{3m}^{-1}\phi_m \tag{29}$$

$$c_{001} = \frac{\partial \phi_B}{\partial z} = \sum_{m=1}^{10} \boldsymbol{X}_{4m}^{-1}\phi_m \tag{30}$$

Therefore, for a general Robin boundary condition at the immersed object surface:

$$\alpha\phi_B + \beta\frac{\partial \phi_B}{\partial n} = f \tag{31}$$

the image point value can be evaluated by satisfying the boundary condition at the boundary point:

$$\phi_I = \frac{f - \sum_{m=2}^{10} M_m\phi_m}{M_0} \tag{32}$$

where M_m is defined according to the following equation, with the components of the normal unit vector indicated as n_x, n_y and n_z respectively:

$$M_m = \alpha \boldsymbol{X}_{1m}^{-1} + \beta\left(n_x \boldsymbol{X}_{2m}^{-1} + n_y \boldsymbol{X}_{3m}^{-1} + n_z \boldsymbol{X}_{4m}^{-1}\right) \quad (33)$$

Considering the correlation between image point and ghost point (Δl is the mutual distance):

$$\phi_B = \frac{\phi_G + \phi_I}{2} \quad (34)$$

$$\frac{\partial \phi_B}{\partial n} = \frac{\phi_G - \phi_I}{\Delta l} \quad (35)$$

the value at the ghost point can be computed as:

$$\phi_G = \frac{\left(2\Delta l M_1 - \alpha\Delta l + 2\beta\right) f + \left(\alpha\Delta l - 2\beta\right)\sum_{m=2}^{10} M_m \phi_m}{\left(\alpha\Delta l + 2\beta\right) M_1} \quad (36)$$

With Equation (36), the matrix coefficients in Equation (19) can be updated. Altered coefficients within the original stencil are incorporated in the implicit scheme, while neighbours outside the original stencil are accounted for in an explicit way. The procedure described above needs to be carried out for all ghost points to ensure that the desired local boundary condition applies everywhere at the immersed boundary surface. Note that the pressure, velocity, concentration and temperature field are obtained for the entire computation domain, i.e. also for the cells inside the particles, with our DNS model proposed above.

RESULTS

In this section, three fluid-solid systems will be presented for coupled heat and mass transfer. The results obtained from our DNS model demonstrate its strong power in engineering applications. In the next sub-sections, comparisons are made between DNS and the "exact" solution for the limiting case of unsteady molecular diffusion and empirical values for forced convection, whereas a three-bead reactor will be considered lastly.

Unsteady mass and heat transport

Here we consider the unsteady diffusion of a certain species to a sphere, where species vanishes and reaction heat is liberated. The sphere is positioned in the centre of a large pool of quiescent fluid. The governing equations for unsteady mass and heat diffusion in the fluid phase are described by Equation (3) and (4) respectively, with $\boldsymbol{u}$ set as zero. The initial conditions are defined by the following two equations, for species and thermal energy conservation equation respectively:

$$c_f = c_{f,0} \quad (37)$$

$$T_f = T_{f,0} \quad (38)$$

The boundary conditions are:

$$c_f\big|_{wall,t} = c_{f,0} \quad (39)$$

$$T_f\big|_{wall,t} = T_{f,0} \quad (40)$$

at the boundaries of the simulation domain, and

$$c_f\big|_{R_s,t} = 0 \quad (41)$$

$$T_f\big|_{R_s,t} = T_s \quad (42)$$

at the sphere surface. Equation (39) and (40) are valid as long as the diffusion fronts have not reached the confining walls. The particle temperature T_s in Equation (42) serves as a dynamic boundary condition for the fluid phase thermal energy equation, and governed by the particle thermal energy equation (Equation (5)).

For the DNS the particle is located in the centre of a cubic box with a length of 0.12m. The data used for the numerical simulation are given in Table 1. The simulation is computed in a 120×120×120 grid with uniform grid spacing in all directions.

Table 1: Data used for the simulation of unsteady mass and heat transport.

Parameter	Value
Time step [s]	5×10^{-5}
Sphere diameter [m]	0.015
Fluid density [kg/m^3]	1.0
Fluid diffusivity [m^2/s]	2×10^{-5}
Fluid thermal conductivity [W/m/K]	0.025
Fluid heat capacity [J/kg/K]	1000
Particle volumetric heat capacity [J/m^3/K]	1000
Reaction enthalpy [J/mol]	-10^{-5}
Fluid initial concentration [mol/m^3]	1.0
Fluid initial temperature [K]	293
Particle initial temperature [K]	293

To offer an "exact" solution for the particle temperature as well as concentration and temperature profiles in the fluid phase, the model composed the spherical symmetric problem (so only r dependence) is solved by a standard second order finite difference technique. In this case, the governing equations for unsteady mass and heat diffusion in the fluid phase are respectively described as:

$$\frac{\partial c_f}{\partial t} = \frac{D_f}{r^2}\frac{\partial}{\partial r}\left(r^2 \frac{\partial c_f}{\partial r}\right) \quad (43)$$

$$\rho_f C_{p,f} \frac{\partial T_f}{\partial t} = \frac{\lambda_f}{r^2}\frac{\partial}{\partial r}\left(r^2 \frac{\partial T_f}{\partial r}\right) \quad (44)$$

The heat and mass transfer rates required in particle thermal energy equation are redefined as:

$$\Phi_{h,f\to s} = \lambda_f \left.\frac{\partial T_f}{\partial r}\right|_{r=R_s} 4\pi R_s^2 \quad (45)$$

$$\Phi_{m,f\to s} = D_f \left.\frac{\partial c_f}{\partial r}\right|_{r=R_s} 4\pi R_s^2 \quad (46)$$

It should be noted here that a very large number of grid points in the radial direction was used to obtain this highly accurate numerical solution. In theory, the particle temperature at final steady state can be computed by Equation (8), which gives:

$$T_s = T_{f,0} + \frac{\Delta T_a}{Le} \quad (47)$$

In this equation, ΔT_a is the adiabatic temperature rise calculated as:

$$\Delta T_a = \frac{\left(-\Delta H_r\right) c_{f,0}}{\rho_f C_{p,f}} \quad (48)$$

and Le is the Lewis number defined as the ratio of the thermal diffusivity and the mass diffusivity:

$$Le = \frac{\frac{\lambda_f}{\rho_f C_{p,f}}}{D_f} = \frac{Sc}{Pr} \tag{49}$$

The simulation results obtained from DNS are compared with the "exact" solution obtained from the standard second order finite difference technique. Using the data listed in Table 1 the analytical temperature difference between the particle and the infinite far fluid is 80K at final steady state. From our DNS, a value of 81.6K is obtained, which matches well with the analytical one. In Figure 2, the particle temperature evolution profiles are plotted along the time scale, to give a comparison between the solutions. As clearly demonstrated in Figure 2, these two solutions reach a good agreement. The behaviour of the evolution curve can be explained as follows. At initial few time steps, the species flux is relatively high so that the heat liberated from the exothermal reaction rapidly heats the particle up from initial temperature. After that, a temperature difference between the particle and the surrounding fluid is established, so that the heat is transferred from the particle to the fluid through unsteady heat conduction. Finally, the heat removal rate goes to the same value as the heat liberation rate, which leads to the final steady state of a constant particle temperature.

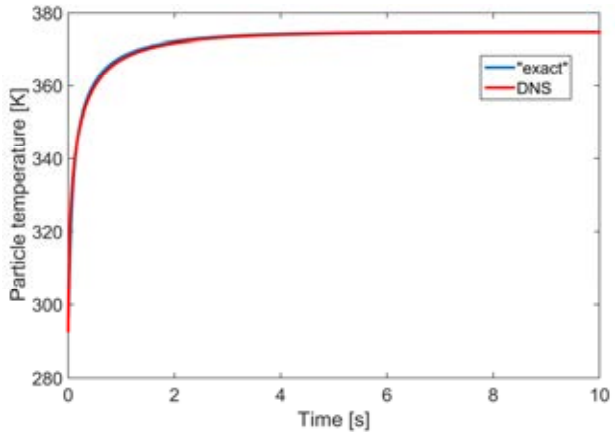

Figure 2: Comparison of particle temperature evolution profiles between simulation and the "exact" solution.

Convective heat and mass transfer to a stationary sphere

In this system, we consider an exothermic chemical reaction under forced convection, which is external mass transfer limited and proceeds at the surface of a single stationary sphere in an enclosure. The sphere is located at the centre of the domain laterally while it is positioned at a distance of two times of the sphere size from the inlet in the flow direction. The data used for the numerical simulation are summarized in Table 2. The simulations are computed in a 240×240×240 grid with uniform grid spacing in all directions. The ratio of domain size to the particle size is eight whereas the mesh resolution applied to the particle is thirty.

The particle Sherwood number Sh_s and Nusselt number Nu_s are predicted by the well-known empirical Frössling and Ranz-Marshall correlations for a single sphere subject to a Dirichlet boundary condition:

$$Sh_s = \frac{k_m d_s}{D_f} = 2.0 + 0.6\left(Re_s\right)^{\frac{1}{2}}\left(Sc\right)^{\frac{1}{3}} \tag{50}$$

$$Nu_s = \frac{\alpha_h d_s}{\lambda_f} = 2.0 + 0.6\left(Re_s\right)^{\frac{1}{2}}\left(Pr\right)^{\frac{1}{3}} \tag{51}$$

where Re_s is the particle Reynolds number, Sc and Pr are the Schmidt number and Prandtl number, respectively. These three dimensionless numbers are defined as follows:

$$Re_s = \frac{\rho_f u_0 d_s}{\mu_f} \tag{52}$$

$$Sc = \frac{\mu_f}{\rho_f D_f} \tag{53}$$

$$Pr = \frac{\mu_f C_{p,f}}{\lambda_f} \tag{54}$$

Table 2: Data used for the simulations of coupled heat and mass transfer to a single stationary sphere under forced convection.

Parameter	Value
Time step [s]	1×10^{-4}
Grid size [m]	5×10^{-4}
Sphere diameter [m]	0.015
Fluid density [kg/m^3]	1.0
Fluid viscosity [kg/m/s]	2×10^{-5}
Fluid diffusivity [m^2/s]	2×10^{-5}
Fluid thermal conductivity [W/m/K]	0.025
Fluid heat capacity [J/kg/K]	1000
Particle volumetric heat capacity [J/m^3/K]	1000
Reaction enthalpy [J/mol]	-10^{-5}
Fluid initial concentration [mol/m^3]	1.0
Fluid initial temperature [K]	293
Particle initial temperature [K]	293

As explained in the second section, the particle temperature at final steady state is described by:

$$\Phi_{m,f\to s}\left(-\Delta H_r\right) = -\Phi_{h,f\to s} \tag{55}$$

The empirical value can be calculated from the mass transfer coefficient k_m and heat transfer coefficient α_h.

$$S_s k_m \left(c_f - c_{f,s}\right)\left(-\Delta H_r\right) = -S_s \alpha_h \left(T_s - T_f\right) \tag{56}$$

where S_s is the particle surface area and $c_{f,s}$ is zero considering the precondition of a completely mass transfer limited chemical reaction proceeding at the sphere surface. Equation (56) can be rearranged to the following expression:

$$T_s = T_f + \frac{k_m c_f \left(-\Delta H_r\right)}{\alpha_h} \tag{57}$$

Substitute Equation (50) and (51) into above equation, the steady state particle temperature can be calculated empirically:

$$T_s = T_f + \frac{Sh_s}{Nu_s}\frac{c_f\left(-\Delta H_r\right)}{\rho_f C_{p,f} Le} \tag{58}$$

In Table 3, the comparison between the simulation results obtained from our DNS model and the empirical values

(indicated as EMP) calculated from Equation (58) is demonstrated. In this table, we also list the particle Sherwood number and Nusselt number calculated from simulation work and the values given by the empirical correlations (Equation (50) and (51)). All results reach a good agreement.

Table 3: Comparison of steady state particle temperature, particle Sherwood number and Nusselt number between DNS and empirical values.

Re_s	T_s		Sh_s		Nu_s	
	DNS	EMP	DNS	EMP	DNS	EMP
30	377.7	376.7	5.13	5.29	4.83	5.05
60	378.4	377.2	6.52	6.65	6.11	6.31
120	379.1	377.7	8.51	8.57	7.91	8.10
240	379.8	378.0	11.53	11.30	10.63	10.63
480	379.9	378.3	15.60	15.15	14.28	14.20

It should be noted here, the particle temperature at final steady state is found to be insensitive to the change of particle Reynolds number. This can be explained by Equation (58). In case of high fluid velocity, the convection term dominates so that the equation can be simplified to the following one, which is independent of particle Reynolds number.

$$T_s = T_f + \frac{(Sc)^{\frac{1}{3}}}{(Pr)^{\frac{1}{3}}} \frac{c_f\left(-\Delta H_r\right)}{\rho_f C_{p,f} Le} = T_f + \frac{c_f\left(-\Delta H_r\right)}{\rho_f C_{p,f} Le^{\frac{2}{3}}} \qquad (59)$$

An in-line array of three stationary spheres

In this sub-section, we consider an in-line array of three spheres, the so-called three-bead reactor. The spheres are positioned in a cuboid domain with 0.21m in length and 0.02m in cross-sectional diameter. Free slip boundary condition is applied at the domain boundary for velocity calculation, while Neumann boundary condition (non-penetrating walls) is used for concentration and thermal energy equations. The first sphere is located at a distance of two times of the sphere size from the inlet in the flow direction, and the other two spheres are located in such a way that the mutual distance between all sphere centres is one and half times of the sphere diameter. Table 4 lists the simulation data.

Table 4: Data used for the simulations of coupled heat and mass transfer in a three-bead reactor.

Parameter	Value
Domain size in grid points	420×40×40
Time step [s]	1×10^{-4}
Grid size [m]	5×10^{-4}
Sphere diameter [m]	0.015
Fluid density [kg/m^3]	1.0
Fluid viscosity [kg/m/s]	2×10^{-5}
Fluid diffusivity [m^2/s]	2×10^{-5}
Fluid thermal conductivity [W/m/K]	0.025
Fluid heat capacity [J/kg/K]	1000
Particle volumetric heat capacity [J/m^3/K]	1000
Reaction enthalpy [J/mol]	-10^{-5}
Fluid initial concentration [mol/m^3]	0.0
Fluid initial temperature [K]	293
Particle initial temperature [K]	293
Fluid inlet velocity [m/s]	0.32
Fluid inlet concentration [mol/m^3]	1.0
Fluid inlet temperature [K]	293

For this three-bead reactor system, we consider two cases. One is of a fast exothermal chemical reaction proceeding at the surface of all three spheres (Case 1), whereas the other one contains an inert (non-reactive) sphere which is located at the second position (Case 2).

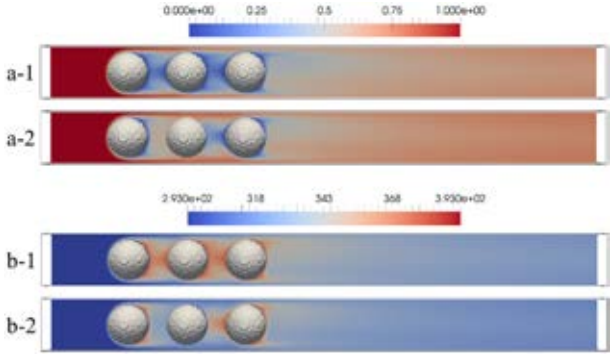

Figure 3: Fluid phase species concentration (a) and thermal temperature (b) distribution inside the reactor, in the central plane. Index 1 and 2 refer to Case 1 and 2 respectively.

Figure 3 illustrates the simulation results of concentration and temperature distribution at steady state for both cases. The corresponding particle temperature evolution profiles are presented in Figure 4. A thermal energy wave is moving through the in-line array of three spheres. The first sphere rapidly heats up due to the exothermal chemical reaction proceeding at its surface. Due to a temperature difference between the particle and the surrounding fluid, the thermal energy is transferred from the solid phase to the fluid phase. The sphere temperature finally reaches a constant value when the removed heat equals to the generated reaction heat. For the first particle, the thermal behavior is almost identical for Case 1 and Case 2. For the second sphere, it has completely different behaviors as it is reactive in Case 1 while an inert surface is assumed in Case 2. For Case 1, there are two contributors to the rise of sphere temperature: liberated reaction heat and convective heat transfer. The unconverted reactant which has passed the first sphere is partly converted at the surface of the second sphere. The thermal energy transferred from the first sphere to the fluid is further transferred to the second sphere. For Case 2, the only heat source is the convective heat transfer as there is no reaction proceeding at the sphere surface. Due to the initial large temperature difference between the fluid and the sphere, it heats up quickly and as a consequence the temperature difference decreases and finally the second sphere reaches the same temperature as the surrounding fluid. For the third sphere, it has the same boundary condition in Case 1 and Case 2. The remaining reactant is partly converted at the surface of the particle and the thermal energy in solid phase is subsequently transferred to the fluid. However, slight differences are noticed in the temperature evolution curves of the third sphere. The particle temperature develops faster in Case 2. This can be explained by the larger driving force of the chemical reaction as the second sphere does not consume any reactant in Case 2. It should be noted that the thermal energy in fluid phase is only generated by the first sphere and partly used for heating up the second sphere in Case 2, which means the convective heat transfer from fluid to the third sphere is

lower comparing with the case of both first and second sphere contributing to the fluid thermal energy in Case 1. This demonstrates the dominant role of reaction heat in the development of particle temperature.

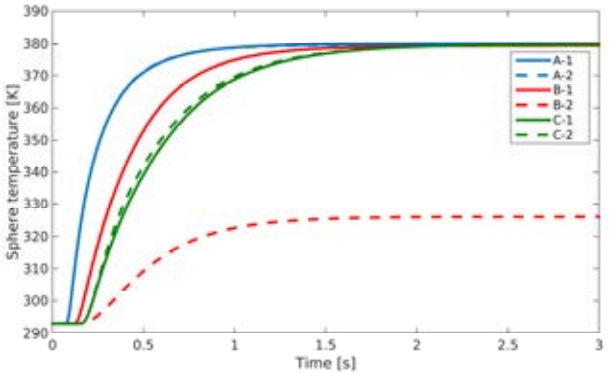

Figure 4: Evolution of particle temperatures for the three-bead reactor. A, B and C are the first, second and third sphere respectively, and index 1 and 2 correspond to Case 1 and 2 respectively.

The axial profiles of cup-average concentration and temperature are shown in Figure 5, which demonstrates the relative contribution of individual sphere to the overall reactant conversion and temperature rise. In both cases, the first sphere has the highest contribution. In Case 1, the second sphere has a lower contribution compared to the first sphere, while the third sphere contributes even less. In Case 2, as expected, the second sphere has no contribution to the reactant conversion and temperature rise. It can be seen from the figure that, both profiles maintain nearly constant between the first sphere and the third sphere. However, the third sphere in Case 2 is noticed to have a higher contribution compared to the second sphere in Case 1. Excluding the influence of concentration driving force, this can be explained by the increased mass transfer rate as no sphere is behind the third sphere, which allows the full development of the fluid flow.

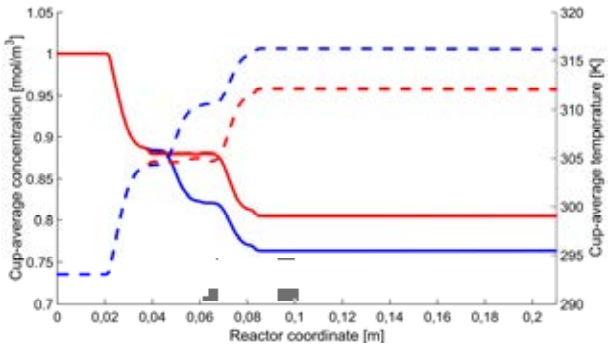

Figure 5: Fluid phase cup-average concentration and temperature profiles along the flow direction. The blue curves are of Case 1 while the red curves are of Case 2. The solid line and the dashed line stand for concentration and temperature respectively.

From the simulation, the overall conversion of the reactant in this three-bead reactor is obtained, which is 0.236 and 0.195 for Case 1 and Case 2 respectively. The theoretical fluid outlet temperature can be computed from the adiabatic temperature rise (Equation (60)). The fluid outlet temperatures given by the simulations are 316.2 and 312.1 for Case 1 and Case 2 respectively, which have a good agreement with the theoretically calculated values - 316.6 and 312.5.

$$T_{f,out} = T_{f,in} + \frac{\left(-\Delta H_r\right) c_{f,in} \xi_f}{\rho_f C_{p,f}} \tag{60}$$

In this equation, ξ_f is the ratio of converted species which is obtained from the simulation. The Nusselt numbers and Sherwood numbers of individual sphere at the time moment of 3 second obtained from our simulations are listed in Table 5, which correspond well with the behaviors of individual sphere contribution in Figure 4. The Nusselt number and Sherwood number are computed by the following expressions:

$$Sh = \frac{\Phi_{m,f\to s}}{4\pi R_s^2 c_{f,in}} \frac{d_s}{D_f} \tag{61}$$

$$Nu = \frac{\Phi_{h,f\to s}}{4\pi R_s^2 \left(T_{f,in} - T_s\right)} \frac{d_s}{\lambda_f} \tag{62}$$

It should be noted that the negative Nusselt number in the following table indicates the heat flux is still flowing from the fluid phase to the solid phase.

Table 5: Nusselt numbers and Sherwood numbers of individual sphere at the time moment of 3s.

		Sphere 1	Sphere 2	Sphere 3
Nu	Case 1	12.90	7.67	6.99
	Case 2	13.34	-0.0013	9.21
Sh	Case 1	14.02	8.29	7.59
	Case 2	14.46	0.00	10.01

CONCLUSION AND FUTURE WORK

In this paper a ghost-cell based immersed boundary method is presented for direct numerical simulation of coupled heat and mass transfer process in fluid-solid systems. In this method, a quadratic interpolation scheme is applied and the boundary condition is incorporated into the governing equations at the discrete level implicitly. Considering an external mass transfer limited exothermal reaction proceeding at the sphere surface, the heat and mass transport is coupled through the particle temperature.

For the case of single sphere unsteady diffusion, the temperature rise of the sphere obtained from DNS has a good agreement with the value calculated theoretically, and the simulation result of particle temperature evolution agrees well with the "exact" solution obtained from a numerical solution using a standard second-order finite difference technique. After that, forced convection to a stationary sphere is considered, the steady state particle temperature matches the empirical value well which is calculated from the mass transfer coefficient and heat transfer coefficient. Besides that, the particle Sherwood number and Nusselt number obtained from DNS are compared with those values given by the well-known empirical Frössling and Ranz-Marshall correlations. In the last simulation, a three-bead reactor is studied which is composed of an in-line array of three spheres. One case consists only of active spheres while the other case assumes the middle sphere is inert. The

temperature evolution of individual particle together with the cup-average concentration and temperature profiles along the flow direction give a detailed description of the behavior of the reactor system. The adiabatic temperature rise obtained from DNS is in good agreement with the value computed from the overall species conversion.

Based on the examples discussed in this work, it is evident that DNS models are a powerful tool to obtain improved correlations for interfacial transfer which could be applied in coarser scale models. The three fluid-solid systems presented in this paper serve as good verifications for our proposed model of coupled heat and mass transfer. Further work related to the extension of the current model to random arrays of particles is ongoing, where more parameters, such as Reynolds number, Damköhler number and solid phase packing density, are of high interest.

ACKNOWLEDGEMENTS

This work was supported by the Netherlands Center for Multiscale Catalytic Energy Conversion (MCEC), an NWO Gravitation programme funded by the Ministry of Education, Culture and Science of the government of the Netherlands.

REFERENCE

BAGCHI, P., HA, M.Y. and BALACHANDAR, S., (2000), "Direct Numerical Simulation of Flow and Heat Transfer From a Sphere in a Uniform Cross-Flow", *J. Fluids Eng.,* **123(2)**, 347-358.

DEEN, N.G., KRIEBITZSCH, S.H.L., VAN DER HOEF, M.A. and KUIPERS, J.A.M., (2012), "Direct numerical simulation of flow and heat transfer in dense fluid–particle systems", *Chem. Eng. Sci.,* **81(0)**, 329-344.

DEEN, N.G. and KUIPERS, J.A.M., (2013), "Direct Numerical Simulation of Fluid Flow and Mass Transfer in Dense Fluid–Particle Systems", *Ind. Eng. Chem. Res.,* **52(33)**, 11266-11274.

DEEN, N.G. and KUIPERS, J.A.M., (2014), "Direct numerical simulation of fluid flow accompanied by coupled mass and heat transfer in dense fluid–particle systems", *Chem. Eng. Sci.,* **116(0)**, 645-656.

DIERICH, F., NIKRITYUK, P.A. and ANANIEV, S., (2011), "2D modeling of moving particles with phase-change effect", *Chem. Eng. Sci.,* **66(22)**, 5459-5473.

FADLUN, E.A., VERZICCO, R., ORLANDI, P. and MOHD-YUSOF, J., (2000), "Combined Immersed-Boundary Finite-Difference Methods for Three-Dimensional Complex Flow Simulations", *J. Comput. Phys.,* **161(1)**, 35-60.

GHIAS, R., MITTAL, R. and DONG, H., (2007), "A sharp interface immersed boundary method for compressible viscous flows", *J. Comput. Phys.,* **225(1)**, 528-553.

GOLDSTEIN, D., HANDLER, R. and SIROVICH, L., (1993), "Modeling a No-Slip Flow Boundary with an External Force Field", *J. Comput. Phys.,* **105(2)**, 354-366.

HAUGEN, N.E.L. and KRAGSET, S., (2010), "Particle impaction on a cylinder in a crossflow as function of Stokes and Reynolds numbers", *J. Fluid Mech.,* **661**, 239-261.

LEE, J. and YOU, D., (2013), "An implicit ghost-cell immersed boundary method for simulations of moving body problems with control of spurious force oscillations", *J. Comput. Phys.,* **233**, 295-314.

LI, X., CAI, J., XIN, F., HUAI, X. and GUO, J., (2013), "Lattice Boltzmann simulation of endothermal catalytic reaction in catalyst porous media", *Appl. Therm. Eng.,* **50(1)**, 1194-1200.

MARELLA, S., KRISHNAN, S., LIU, H. and UDAYKUMAR, H.S., (2005), "Sharp interface Cartesian grid method I: An easily implemented technique for 3D moving boundary computations", *J. Comput. Phys.,* **210(1)**, 1-31.

MOHD-YUSOF, J., (1997), "Combined Immersed-Boundary and B-spline methods for simulations of flow in complex geometries", *Cen. Turb. Res.,* **Annual Research Brief**, 317-327.

PESKIN, C.S., (1977), "Numerical analysis of blood flow in the heart", *J. Comput. Phys.,* **25(3)**, 220-252.

SAIKI, E.M. and BIRINGEN, S., (1996), "Numerical Simulation of a Cylinder in Uniform Flow: Application of a Virtual Boundary Method", *J. Comput. Phys.,* **123(2)**, 450-465.

SEO, J.H. and MITTAL, R., (2011), "A high-order immersed boundary method for acoustic wave scattering and low-Mach number flow-induced sound in complex geometries", *J. Comput. Phys.,* **230(4)**, 1000-1019.

SHU, C., LI, X., REN, W.W. and YANG, W.M., (2013), "Novel immersed boundary methods for thermal flow problems", *Int. J. Numer Method H,* **23(1)**, 124-142.

TAVASSOLI, H., KRIEBITZSCH, S.H.L., VAN DER HOEF, M.A., PETERS, E.A.J.F. and KUIPERS, J.A.M., (2013), "Direct numerical simulation of particulate flow with heat transfer", *Int. J. Multiphase Flow,* **57(0)**, 29-37.

TENNETI, S., SUN, B., GARG, R. and SUBRAMANIAM, S., (2013), "Role of fluid heating in dense gas–solid flow as revealed by particle-resolved direct numerical simulation", *Int. J. Heat Mass Transfer,* **58(1–2)**, 471-479.

TSENG, Y.-H. and FERZIGER, J.H., (2003), "A ghost-cell immersed boundary method for flow in complex geometry", *J. Comput. Phys.,* **192(2)**, 593-623.

UDAYKUMAR, H.S., MITTAL, R., RAMPUNGGOON, P. and KHANNA, A., (2001), "A Sharp Interface Cartesian Grid Method for Simulating Flows with Complex Moving Boundaries", *J. Comput. Phys.,* **174(1)**, 345-380.

UHLMANN, M., (2005), "An immersed boundary method with direct forcing for the simulation of particulate flows", *J. Comput. Phys.,* **209(2)**, 448-476.

VAN DER HOEF, M.A., VAN SINT ANNALAND, M., DEEN, N.G. and KUIPERS, J.A.M., (2008), "Numerical Simulation of Dense Gas-Solid Fluidized Beds: A Multiscale Modeling Strategy", *Annu. Rev. Fluid Mech.,* **40(1)**, 47-70.

WANG, Z., FAN, J., LUO, K. and CEN, K., (2009), "Immersed boundary method for the simulation of flows with heat transfer", *Int. J. Heat Mass Transfer,* **52(19–20)**, 4510-4518.

XIA, J., LUO, K. and FAN, J., (2014), "A ghost-cell based high-order immersed boundary method for inter-phase heat transfer simulation", *Int. J. Heat Mass Transfer,* **75**, 302-312.

ZHANG, N., ZHENG, Z.C. and ECKELS, S., (2008), "Study of heat-transfer on the surface of a circular cylinder in flow using an immersed-boundary method", *Int. J. Heat Fluid Flow,* **29(6)**, 1558-1566.